

Shape of magnetic domain walls formed by coupling to mobile charges

Ryo Ozawa,¹ Satoru Hayami,² Kipton Barros,³ and Yukitoshi Motome¹

¹*Department of Applied Physics, University of Tokyo, Tokyo 113-8656, Japan*

²*Department of Physics, Hokkaido University, Sapporo 060-0810, Japan*

³*Theoretical Division and CNLS, Los Alamos National Laboratory, Los Alamos, New Mexico 87545, U.S.A.*

(Dated: June 7, 2021)

Magnetic domain walls, which are crucially important in both fundamental physics and technical applications, often have a preference in their form due to many different origins, such as the crystalline shape, lattice symmetry, and magnetic anisotropy. We theoretically investigate yet another origin stemming from the coupling to mobile charges in itinerant magnets. Performing a large-scale numerical simulation in a minimal model for itinerant magnets, i.e., the Kondo lattice model with classical localized spins, we show that the shape of magnetic domain walls depends on the electronic band structure and electron filling. While Néel and 120° antiferromagnetic states do not show a strong preference in the shape of domain walls, noncoplanar spin states with scalar chiral ordering have distinct directional preferences of the domain walls depending on the electron filling. We find that the directional preference is rationalized by the wave-number dependence of the effective magnetic interactions induced by the mobile charges, which are set by the band structure and electron filling. We also observe that, in the noncoplanar chiral states, an electric current is induced along the domain walls owing to the spin Berry phase mechanism, with very different spatial distributions depending on whether the bulk state is metallic or insulating.

PACS numbers: 71.10.Fd, 71.27.+a, 75.10.-b

I. INTRODUCTION

Magnetic domain walls (DWs) have been an important issue in both fundamental physics of magnetism and applications to magnetic devices. Besides the phenomenological understanding, it is not easy to establish the microscopic theory for the formation of DWs, as it is basically a nonequilibrium phenomenon with spatial inhomogeneity, often ranging from nano to micrometer scales. Magnetic DWs have been studied mainly in classical spin models with neglecting mobile charges, by considering the effects of, e.g., crystalline shape, lattice symmetry, and magnetic anisotropy^{1–3}. Spatial modulations of spin textures have been clarified near the DWs, such as the so-called Bloch, Néel, and cross-tie walls.

Recently, the magnetic DWs have gained renewed interest through the studies toward functional devices based on, e.g., the giant magnetoresistive effect^{4,5}, spintronics^{6–8}, and multiferroics^{9,10}. An intriguing issue is the current-induced DW motion. The controllability of DWs by an electric current was experimentally demonstrated in itinerant ferromagnets^{11,12}. The microscopic mechanism was theoretically discussed by taking into consideration the interplay between spin and charge degrees of freedom of electrons^{8,13–18}. Another issue discussed very recently is the DWs in topological states of matter. An example has been discussed in the peculiar magnetically ordered state called all-in all-out type in pyrochlore oxides. For instance, in $\text{Cd}_2\text{Os}_2\text{O}_7$, the domain formation was observed using resonant x-ray diffraction, and controllability of the domain structures by a magnetic field-cooling procedure was demonstrated¹⁹. Meanwhile, for iridium pyrochlore oxides, peculiar electronic states were theoretically predicted, such as the Weyl

semimetal²⁰ and peculiar metallic DWs^{21,22}. Experimentally, a hysteresis was observed in the magnetoresistance for $\text{Nd}_2\text{Ir}_2\text{O}_7$, and its relation to the metallic DWs was discussed^{23–25}. Recently, the real-space image of the metallic DWs was observed by microwave impedance microscopy²⁶.

In these DW problems, an interesting fundamental issue is how the shape of DWs is determined in such itinerant magnets. In most of the previous studies, the presence and the shape of DWs were introduced ‘by hand’, and the resultant electronic and magnetic properties were studied. For a microscopic understanding of the DW physics, it is crucial to study the DW formation by treating the spin and charge (and possibly, orbital) degrees of freedom on an equal footing, without posing any assumption on the patterns of DWs. It is also crucial to incorporate spatial, thermal, and quantum fluctuations for further development, including the creation, annihilation, deformation, and movement of DWs. Amongst others, it is strongly desired to enable unbiased calculations of such complicated systems, in spatially large systems ranging up to nano or micrometer scales.

In this paper, as a first step toward such further understanding of DWs in itinerant magnets, we theoretically study the formation of DWs by large-scale numerical simulation including the interplay between spin and charge degrees of freedom. Our purpose is to clarify what types of magnetic domains are formed through the interplay. In particular, our focus is on how the shape of the DWs is determined for the systems with different electronic and lattice structures. We also study the electronic properties near the magnetic DWs.

For this purpose, we consider a minimal model for the spin-charge coupled systems, the Kondo lattice model, which describes mobile charges coupled to classical lo-

calized spins. To enable large-scale simulation, we employ a numerical technique based on the Langevin dynamics (LD) and kernel polynomial method (KPM)²⁷. In Ref. 27, different shapes of the DWs were reported for different electron fillings even for the same magnetic structure, while the origin was not referred. Stimulated by the observation, we here study the DW issue in the Kondo lattice model in a systematic way, using a modified version of the KPM-LD method by applying stochastic Landau-Lifshitz (SLL) dynamics, away from the overdamped limit.

In the present study, we analyze the formation of magnetic domains by performing the modified KPM-LD simulation with a sudden quench from high-temperature limit to zero temperature. We study several different magnetically ordered states appearing in the Kondo lattice models on square and triangular lattices while varying the electron filling. We find that, for the collinear Néel state on the square lattice and coplanar 120° state on the triangular lattice, the DWs do not show a strong preference in their directions in real space. On the other hand, for the noncoplanar spin states with three ordering vectors (triple- Q) on the triangular lattice near 1/4 and 3/4 fillings^{28,29}, we demonstrate that the DWs show very distinct shapes depending on the electron filling, as observed in the previous study²⁷. We also show that spontaneous electric current, which emerges through the spin Berry phase mechanism^{30,31}, flows along the DWs in a different manner between the two cases despite the same magnetic ground states. We show that the distinct directional preference of DWs is brought by the momentum-dependence of effective spin-spin interactions mediated by mobile charges.

The rest of the paper is organized as follows. In Sec. II, we introduce the model and numerical method that we use in the present study. After introducing the Hamiltonian of the Kondo lattice model in Sec. II A, we discuss effective interactions between the localized spins in Sec. II B. We also introduce the method of KPM-LD simulation and its extension in Sec. II C, and a numerical method to evaluate the expectation value of electronic properties in Sec. II D. In Sec. III, we present the numerical results. We show the DW formation in the collinear Néel state on the square lattice (Sec. III A), the coplanar 120° state on the triangular lattice (Sec. III B), and noncoplanar triple- Q states on the triangular lattice (Sec. III C). In Sec. IV, we discuss the origin of the directional preference of DWs from the wave-number dependence of the bare susceptibility $\chi_{\mathbf{q}}^0$. Section V is devoted to summary.

II. MODEL AND METHOD

In this section, we present the model and method that we use. After introducing the Kondo lattice model in Sec. II A, we discuss the effective interaction between the localized spins mediated by mobile charges in Sec. II B. In

Sec. II C, we briefly review the KPM-LD method and introduce its extension by applying the SLL variant of LD. We also review the method to evaluate physical quantities by the KPM in Sec. II D.

A. Kondo Lattice Model

To investigate the DW problem in itinerant magnets, we consider a minimal model describing the interplay between spin and charge degrees of freedom, the Kondo lattice model with classical localized spins. The Hamiltonian is given by

$$\hat{\mathcal{H}} = -t \sum_{\langle i,j \rangle, \sigma} (\hat{c}_{i\sigma}^\dagger \hat{c}_{j\sigma} + \text{H.c.}) - J \sum_i \hat{\mathbf{s}}_i \cdot \mathbf{S}_i - D \sum_i (S_i^z)^2, \quad (1)$$

where $\hat{c}_{i\sigma}^\dagger$ ($\hat{c}_{i\sigma}$) is a creation (annihilation) operator of a mobile charge at site i and spin σ , $\hat{\mathbf{s}}_i = \frac{1}{2} \sum_{\sigma\sigma'} \hat{c}_{i\sigma}^\dagger \boldsymbol{\sigma}_{\sigma\sigma'} \hat{c}_{i\sigma'}$ is the spin operator of a mobile charge [$\boldsymbol{\sigma} = (\sigma^x, \sigma^y, \sigma^z)$ is the vector of Pauli matrices], \mathbf{S}_i denotes a classical localized spin at site i whose amplitude is normalized as $|\mathbf{S}_i| = 1$. In the following study, we consider the model on square and triangular lattices; the sum of $\langle i, j \rangle$ is taken over the nearest-neighbor sites on each lattice. The first term in Eq. (1) represents the hopping of mobile charges between the nearest-neighbor sites with the amplitude $-t$. The second term shows the onsite exchange coupling between the localized spins and spin degree of freedom of mobile charges with the coupling constant J (the sign of J is irrelevant for classical localized spins). The third term represents a uniaxial spin anisotropy with the amplitude D , which comes from, e.g., the relativistic spin-orbit coupling. Hereafter, we take $t = 1$ and $a = 1$ (lattice constant) as energy and length units, respectively.

In the Kondo lattice model in Eq. (1), the coupling to mobile charges leads to an effective magnetic interaction between localized spins. In the strong coupling case ($J \gg t$), $\langle \hat{\mathbf{s}}_i \rangle$ and \mathbf{S}_i are almost in parallel, and the effective hopping amplitude of mobile charges depends on the relative angle of neighboring localized spins^{32,33}. As a consequence, the ferromagnetic ordering is favored to maximize the kinetic energy of mobile charges. The effective ferromagnetic interaction between localized moments is called the double-exchange interaction³². On the other hand, when $J \ll t$, the effective magnetic interaction becomes complicated with oscillating sign depending on the distance between the localized spins. The weak coupling case will be discussed in the following sections.

B. RKKY Interaction

Hereafter, we investigate magnetic DWs in the weak J region of the Kondo lattice model, where various magnetic orderings are expected to occur owing to the effec-

tive magnetic interaction mediated by mobile charges as discussed below. In the weak coupling limit ($J \ll t$), the effective magnetic interaction is derived by the second-order perturbation in terms of J , which is written as

$$\mathcal{H}^{\text{RKKY}} = -\frac{J^2}{4} \sum_{\mathbf{q}} \chi_{\mathbf{q}}^0 |\mathbf{S}_{\mathbf{q}}|^2. \quad (2)$$

Here, $\mathbf{S}_{\mathbf{q}}$ is the Fourier transform of \mathbf{S}_i given by

$$\mathbf{S}_{\mathbf{q}} = \frac{1}{\sqrt{N}} \sum_j \mathbf{S}_j e^{i\mathbf{q} \cdot \mathbf{r}_j}, \quad (3)$$

where N is the number of sites and $\mathbf{r}_j = (r_j^x, r_j^y)$ is the position of the site j . In Eq. (2), $\chi_{\mathbf{q}}^0$ is the bare magnetic susceptibility of mobile charges,

$$\chi_{\mathbf{q}}^0 = -\frac{1}{N} \sum_{\mathbf{k}} \frac{f(\varepsilon_{\mathbf{k}+\mathbf{q}}) - f(\varepsilon_{\mathbf{k}})}{\varepsilon_{\mathbf{k}+\mathbf{q}} - \varepsilon_{\mathbf{k}}}, \quad (4)$$

where $f(\varepsilon)$ is the Fermi distribution function and $\varepsilon_{\mathbf{k}}$ is the dispersion relation of mobile charges with a wave number $\mathbf{k} = (k_x, k_y)$ given by

$$\varepsilon_{\mathbf{k}} = -2(\cos k_x + \cos k_y) \quad (5)$$

for the square lattice and

$$\varepsilon_{\mathbf{k}} = -2 \left[\cos k_x + \cos \left(-\frac{k_x}{2} + \frac{\sqrt{3}k_y}{2} \right) + \cos \left(-\frac{k_x}{2} - \frac{\sqrt{3}k_y}{2} \right) \right] \quad (6)$$

for the triangular lattice.

The interaction in Eq. (2) is called the Ruderman-Kittel-Kasuya-Yosida (RKKY) interaction^{34–36}. The wave number dependence gives rise to a long-range interaction in real space with oscillating sign. Equation (2) provides us a good insight into the magnetic ground state in the Kondo lattice model: as $|\mathbf{S}_{\mathbf{q}}|^2 \geq 0$ and $\sum_{\mathbf{q}} |\mathbf{S}_{\mathbf{q}}|^2 = N$, the ground state will develop a magnetic order specified by the wave number(s) for which $\chi_{\mathbf{q}}^0$ is maximized.

C. Modified KPM-LD Method

To study the magnetic and electronic states in the Kondo lattice model, we employ an efficient numerical technique, the KPM-LD method²⁷. This technique is widely applicable to the systems in which noninteracting fermions are coupled to classical degrees of freedom, and enables us to perform an unrestricted simulation in large-size systems. In the following, we briefly introduce the KPM-LD technique and its most recent modifications that we use here.

In the Kondo lattice model in Eq. (1), the partition function Z is given by

$$Z = \text{Tr}_{\{\mathbf{S}_i\}} \text{Tr}_{\{\hat{c}_i\}} \exp\{-[\mathcal{H}(\{\mathbf{S}_i\}) - \mu \sum_{i\sigma} \hat{c}_{i\sigma}^\dagger \hat{c}_{i\sigma}]/T\} \quad (7)$$

$$= \text{Tr}_{\{\mathbf{S}_i\}} \exp[-\Omega(\{\mathbf{S}_i\})/T], \quad (8)$$

where μ is the chemical potential and T is temperature (we set the Boltzmann constant $k_B = 1$). $\Omega(\{\mathbf{S}_i\})$ is the grand potential for a spin configuration $\{\mathbf{S}_i\}$, which is given by

$$\Omega(\{\mathbf{S}_i\}) = - \int d\varepsilon \rho(\varepsilon; \{\mathbf{S}_i\}) T \log\{1 + \exp[-(\varepsilon - \mu)/T]\}. \quad (9)$$

Here, $\rho(\varepsilon; \{\mathbf{S}_i\})$ is the density of states,

$$\rho(\varepsilon; \{\mathbf{S}_i\}) = \frac{1}{N} \sum_j \delta(\varepsilon - \varepsilon_j(\{\mathbf{S}_i\})), \quad (10)$$

where $\varepsilon_j(\{\mathbf{S}_i\})$ is the j th eigenvalue of the Hamiltonian in Eq. (1) for the spin configuration $\{\mathbf{S}_i\}$. In the KPM-LD algorithm, the trace over $\{\hat{c}_i\}$ in Eq. (7) is evaluated by the KPM and the trace over $\{\mathbf{S}_i\}$ is evaluated by the stochastic sampling of the LD.

In the KPM for the trace over $\{\hat{c}_i\}$, the density of states in Eq. (10) is expanded by the Chebyshev polynomials as

$$\rho(x; \{\mathbf{S}_i\}) \simeq \sum_{m=0}^M g_m^J w_m(x) \mu_m T_m(x), \quad (11)$$

where $T_m(x)$ is the m th-order Chebyshev polynomial. Here, the energy ε is scaled so that all the eigenvalues are within the range $x \in [-1, 1]$, $w_m(x)$ is the weight function for Chebyshev polynomials given by $w_m(x) = (2 - \delta_{0,m})/(\pi\sqrt{1-x^2})$, and μ_m is the Chebyshev moment given by $\mu_m = \text{Tr}[T_m(\mathcal{H}(\{\mathbf{S}_i\}))]$. Following the previous studies, we take the summation in the trace over random vectors, instead of the complete basis set³⁷. To improve the accuracy of the stochastic KPM approximation, we select a set of correlated random vectors using a matrix probing technique³⁸ inspired by Ref. 39. In Eq. (11), M is the truncation number for the Chebyshev polynomial expansion, and g_m^J is the so-called Jackson kernel which suppresses the error due to the truncation³⁷.

Meanwhile, in the LD that generates spin configurations for the trace over $\{\mathbf{S}_j\}$, we modified the algorithm from the original one in Ref. 27 by applying the SLL equation⁴⁰. The SLL equation is

$$\frac{d\mathbf{S}_i}{d\tau} = -\mathbf{S}_i \times \mathbf{H}_i - \alpha \mathbf{S}_i \times (\mathbf{S}_i \times \mathbf{H}_i). \quad (12)$$

The first and second terms represent a precession and dumping of \mathbf{S}_i , respectively; \mathbf{H}_i is the effective magnetic field for \mathbf{S}_i given by

$$\mathbf{H}_i = -\frac{\partial \Omega(\{\mathbf{S}_j\})}{\partial \mathbf{S}_i} + \mathbf{h}_i(\tau, T). \quad (13)$$

Here, the first term on the RHS is numerically evaluated by the automatic differentiation transformation²⁷, and \mathbf{h}_i represents thermal fluctuations, which satisfies $\langle h_i^{\nu_1}(\tau_1, T) h_j^{\nu_2}(\tau_2, T) \rangle_\tau = 2T\delta(\tau_1 - \tau_2)\delta_{ij}\delta_{\nu_1\nu_2}$, where $\langle \dots \rangle_\tau$ is the time average and h_i^ν is the ν component of \mathbf{h}_i .

For the time evolution, we use the Heun integration scheme, a type of predictor-corrector method, to achieve second-order accuracy with respect to $\Delta\tau$ (time interval of the update of spins). Note that the SLL equation, Eq. (12), preserves the length of spins, i.e., $|\mathbf{S}_i| = 1$. However, numerical errors in the Heun scheme violate this condition at order $\mathcal{O}(\Delta\tau^2)$. To improve accuracy, we rescale the spin lengths at each time step, which implements the so-called Heun+projection scheme⁴¹.

The computational cost of the modified KPM-LD simulation for an update of all the spins is $\mathcal{O}(N)$, similar to the original KPM-LD²⁷. This is much smaller than the cost of the conventional Monte Carlo algorithm, $\mathcal{O}(N^4)$ ⁴². This drastic reduction of computational cost enables the simulation of systems with $\sim 10^4$ sites, whereas the conventional algorithm would be limited to several hundred sites.

In the following, we use the modified KPM-LD method introduced above. In the calculations, we set $\alpha = 1$ and $\Delta\tau = 20$ in the SLL equation⁴³, and perform the Chebyshev polynomial expansion up to $M = 2000$ with using 144 correlated random vectors for the KPM. We perform the simulation at $T = 0$ starting from a random spin configuration, which corresponds to a sudden quench from the high- T limit to zero T . In the following, we show the results for the system size $N = 120^2$ for both the square and triangular-lattice cases. We confirmed that qualitatively the same results are obtained for several different random samples and for smaller size systems, $N = 60^2$ and 90^2 . In the simulation, we use General-Purpose computing on Graphics Processing Units (GPGPU) to perform the sparse matrix operations required for the KPM approximation of the effective field, Eq. (13).

D. Physical Quantities

In this section, we show how to evaluate physical quantities for mobile electrons by the KPM^{37,44}, such as local charge and current densities. The expectation value of an operator \hat{A} for a given spin configuration $\{\mathbf{S}_j\}$ is obtained as

$$\langle \hat{A} \rangle = \sum_i \langle i | \hat{A} | i \rangle f(\varepsilon_i(\{\mathbf{S}_j\})) = \int d\varepsilon A(\varepsilon; \{\mathbf{S}_j\}) f(\varepsilon), \quad (14)$$

where $\{|i\rangle\}$ is the complete set of single-particle electron eigenstates of the Kondo lattice model for $\{\mathbf{S}_j\}$, and

$A(\varepsilon; \{\mathbf{S}_j\})$ is defined by

$$\begin{aligned} A(\varepsilon; \{\mathbf{S}_j\}) &= \sum_i \delta(\varepsilon - \varepsilon_i(\{\mathbf{S}_j\})) \langle i | \hat{A} | i \rangle \\ &= \sum_i \langle i | \delta(\varepsilon - \hat{\mathcal{H}}(\{\mathbf{S}_j\})) \hat{A} | i \rangle. \end{aligned} \quad (15)$$

Similar to Eq. (11), we can estimate $A(\varepsilon; \{\mathbf{S}_j\})$ by the KPM as

$$A(x; \{\mathbf{S}_j\}) \simeq \sum_{m=0}^M g_m^J w_m(x) \mu_m^A T_m(x), \quad (16)$$

where μ_m^A is the moment in the Chebyshev polynomial expansion. Using the orthonormality of $T_m(x)$, μ_m^A is obtained as

$$\begin{aligned} \mu_m^A &= \int dx T_m(x) A(x; \{\mathbf{S}_j\}) \\ &= \int dx \sum_i \langle i | T_m(x) \delta(x - \hat{\mathcal{H}}(\{\mathbf{S}_j\})) \hat{A} | i \rangle \\ &= \sum_i \langle i | T_m(\hat{\mathcal{H}}(\{\mathbf{S}_j\})) \hat{A} | i \rangle \\ &= \text{Tr}[T_m(\hat{\mathcal{H}}(\{\mathbf{S}_j\})) \hat{A}]. \end{aligned} \quad (17)$$

Equation (17) is calculated by massive vector-matrix products, whose computational cost is $\mathcal{O}(N^2)$ when the complete basis set is used. However, if \hat{A} is a local operator, e.g., the one defined for a site, bond, or plaquette, it only requires $\mathcal{O}(N)$ cost because the sum of i in Eq. (17) is limited to the sites where \hat{A} is defined.

III. NUMERICAL RESULTS

In this section, we examine the shape of magnetic domains in the Kondo lattice model by the modified KPM-LD simulation. In Secs. III A and III B, we present the results for the collinear Néel state on the square lattice and the coplanar 120° state on the triangular lattice, respectively. In Sec. III C, we show the results for noncoplanar triple- Q states with scalar chiral ordering which are stabilized near 1/4 and 3/4 fillings on the triangular lattice. We also present how the spontaneous electric current by the spin Berry phase mechanism flows along the DWs in each case. In each section, we present the wave-number dependence of the bare susceptibility $\chi_{\mathbf{q}}^0$ in Eq. (4). The relation between $\chi_{\mathbf{q}}^0$ and the anisotropy of DWs in real space will be discussed in Sec. IV.

A. Collinear Néel State

Let us first discuss the case of the Néel state, which is a collinear antiferromagnetic (AFM) state. It is stabilized in the Kondo lattice model on the square lattice near half filling because of the perfect nesting of the Fermi surface

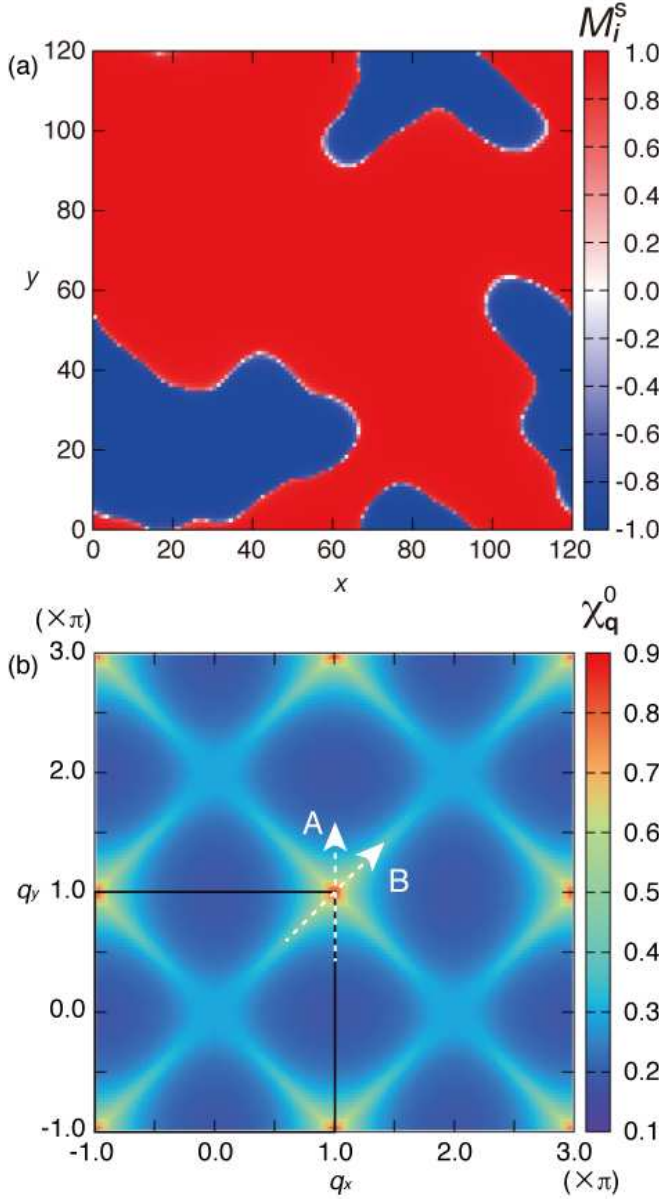


FIG. 1. (Color online) (a) Real-space distribution of the staggered magnetization M_i^s obtained by the modified KPM-LD simulation for the Kondo lattice model on the square lattice at $\mu = 0$ ($n \sim 0.5$), $J = 0.2$, $D = 0.005$, and $N = 120^2$. (b) Bare susceptibility χ_q^0 at $\mu = 0$ in the momentum space. The black square represents the 1st BZ. The arrows A and B denote the cuts along which we evaluate the second derivative of χ_q^0 ; see Sec. IV for details.

with the (π, π) ordering vector. The spatial pattern of the localized spins is represented by

$$\mathbf{S}_i = \begin{pmatrix} 0 \\ 0 \\ (-1)^{r_i^x + r_i^y} \end{pmatrix}. \quad (18)$$

We investigate what type of the domain structures is realized in the Néel state by the modified KPM-LD simulation.

Figure 1(a) shows a snapshot of domain structure in the Néel state obtained by the modified KPM-LD simulation for the square lattice system with $N = 120^2$ under periodic boundary conditions. We set $\mu = 0$ to realize the half filling, $n \sim 0.5$ [$n = \sum_{i\sigma} \langle \hat{c}_{i\sigma}^\dagger \hat{c}_{i\sigma} \rangle / (2N)$], and take $J = 0.2$. Figure 1(a) represents the real-space configuration of the staggered magnetization, $M_i^s = (-1)^{i_x + i_y} S_i^z$, at $\tau = 2 \times 10^3$; we here introduced a small positive $D = 0.005$ to observe the domains in a clear form. In the figure, there are three domains separated by the DWs. The DWs have overall round shapes, while we can see a weak preference along the diagonal directions compared to the horizontal and vertical directions.

Figure 1(b) shows the corresponding bare susceptibility χ_q^0 defined in Eq. (4), calculated at $\mu = 0$ and $T = 0.05$ for $N = 600^2$. As expected from the perfect nesting property, χ_q^0 exhibits a sharp peak at $\mathbf{q} = (\pi, \pi)$ in the first Brillouin zone (1st BZ), which grows to a δ function in the limit of $T \rightarrow 0$ and $N \rightarrow \infty$. The peak is weakly anisotropic in the momentum space between the vertical (A) and diagonal (B) directions. The relation between the structure of χ_q^0 near the peaks and the shape of DWs will be discussed in Sec. IV.

B. Coplanar 120° State

Next, we consider the case for a noncollinear but coplanar 120° AFM state on the triangular lattice. The spin configuration is typically described by

$$\mathbf{S}_i = \begin{pmatrix} \cos(\mathbf{Q}_K \cdot \mathbf{r}_i) \\ \sin(\mathbf{Q}_K \cdot \mathbf{r}_i) \\ 0 \end{pmatrix}, \quad (19)$$

where \mathbf{Q}_K denotes the wave number at the K point in the 1st BZ: $\mathbf{Q}_K = (\frac{4}{3}\pi, 0)$ or $(\frac{2}{3}\pi, \frac{2}{\sqrt{3}}\pi)$ [see Fig. 2(b)]. The 120° AFM order is regarded as a ferroic order of the vector chirality defined as

$$\chi_p^{\text{vc}} = \mathbf{S}_{p_1} \times \mathbf{S}_{p_2} + \mathbf{S}_{p_2} \times \mathbf{S}_{p_3} + \mathbf{S}_{p_3} \times \mathbf{S}_{p_1}, \quad (20)$$

where p_1 , p_2 , and p_3 are the sites on each triangular plaquette p in a counterclockwise direction. We use the vector chirality to characterize the domains in the 120° AFM state.

Figure 2(a) shows a snapshot of the vector chirality obtained by the modified KPM-LD simulation for the triangular lattice system with $N = 120^2$ under periodic boundary conditions. We set $\mu = -0.95$ ($n \sim 0.31$) to stabilize the 120° AFM order, and take $J = 0.2$. The plot shows the z component of the vector chirality in Eq. (20), $(\chi_p^{\text{vc}})^z$, at $\tau = 3.2 \times 10^4$; we introduced a small negative $D = -0.005$ to clearly observe the domains. There are two domains with positive and negative $(\chi_p^{\text{vc}})^z$ separated by one DW, as shown in Fig. 2(a). The typical spin

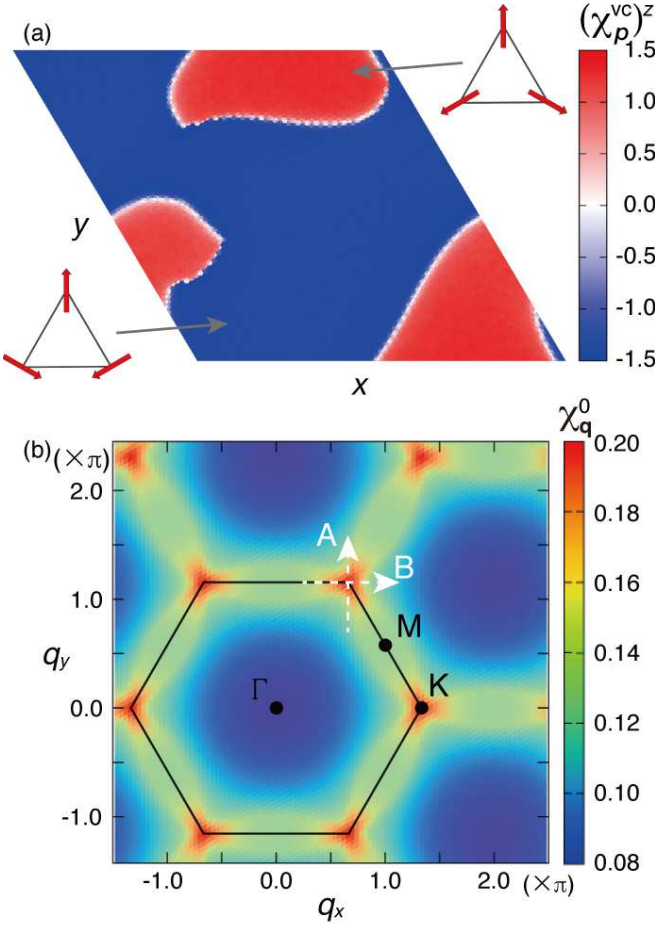


FIG. 2. (Color online) (a) Real-space distribution of the z component of the vector chirality χ_p^{vc} obtained by the modified KPM-LD simulation on the triangular lattice at $\mu = -0.95$ ($n \sim 0.31$), $J = 0.2$, and $D = -0.005$ for $N = 120^2$. The inset shows the schematic pictures of spin patterns for the positive and negative $(\chi_p^{vc})^z$ on triangular plaquettes. (b) Bare susceptibility χ_q^0 at $\mu = -0.95$ in the momentum space. The black hexagon represents the 1st BZ. The arrows A and B denotes the cuts along which we evaluate the second derivative of χ_q^0 ; see Sec. IV for details.

patterns in each domain are shown in the inset. The DW has a round shape and does not show the strong preference in the direction.

Figure 2(b) shows the corresponding bare susceptibility χ_q^0 in Eq. (4) evaluated at $\mu = -0.95$ and $T = 0.05$ for $N = 600^2$. χ_q^0 exhibits a distinct peak at the K point in the 1st BZ, which is consistent with the stabilization of 120° ordering. The structure of χ_q^0 near the peak is nearly isotropic with threefold rotational symmetry. We will return to this point in Sec. IV.

C. Noncoplanar Triple-Q States

In this section, we consider the case for a triple-Q AFM state. The triple-Q state is characterized by three ordering vectors, whose spin pattern is typically given by

$$\mathbf{S}_i = \frac{1}{\sqrt{3}} \begin{pmatrix} \cos(\mathbf{Q}_{M_1} \cdot \mathbf{r}_i) \\ \cos(\mathbf{Q}_{M_2} \cdot \mathbf{r}_i) \\ \cos(\mathbf{Q}_{M_3} \cdot \mathbf{r}_i) \end{pmatrix}. \quad (21)$$

Here, \mathbf{Q}_{M_ℓ} ($\ell = 1, 2, 3$) denote the three ordering vectors: $\mathbf{Q}_{M_1} = (\pi, \frac{1}{\sqrt{3}}\pi)$, $\mathbf{Q}_{M_2} = (0, \frac{2}{\sqrt{3}}\pi)$, and $\mathbf{Q}_{M_3} = (-\pi, \frac{1}{\sqrt{3}}\pi)$, which correspond to the M points in the 1st BZ. Thus, the triple-Q order has a noncoplanar spin pattern with four-sublattice unit cell, as shown in the inset of Fig. 3(a). This peculiar order takes place in the Kondo lattice model on the triangular lattice near $3/4$ and $1/4$ fillings: the former is stabilized by the perfect nesting of the Fermi surface at $3/4$ filling²⁸, while the latter by a partial nesting near $1/4$ filling^{45,46}. The noncoplanar triple-Q states accompany a ferroic order of scalar chirality,

$$\chi_p^{sc} = \mathbf{S}_{p_1} \times \mathbf{S}_{p_2} \cdot \mathbf{S}_{p_3}, \quad (22)$$

defined on the triangular plaquette p , as in Eq. (20). χ_p^{sc} acts as a Z_2 variable even when the Hamiltonian preserves the $SO(3)$ symmetry. We use χ_p^{sc} to characterize the magnetic domains in the triple-Q AFM states near $1/4$ and $3/4$ fillings in the following.

Figure 3(a) shows a snapshot of the scalar chirality in the triple-Q ordered state near $1/4$ filling, obtained by the modified KPM-LD simulation for the triangular lattice system with $N = 120^2$ under periodic boundary conditions. We set $\mu = -2$ ($n \sim 0.22$) and take $J = 0.2$ and $D = 0$. The figure represents the real-space configuration at $\tau = 8 \times 10^4$. Unlike the cases of the Néel and 120° states, DWs have a strong preference in their directions; they prefer three directions, all of which are perpendicular to the nearest-neighbor bonds of the triangular lattice.

Figure 3(b) shows the result for the triple-Q state near $3/4$ filling. We set $\mu = 2$ ($n \sim 0.75$) and take the same values for the other parameters as in Fig. 3(a). While the system exhibits several domains as in Fig. 3(a), the directions of DWs exhibit a different preference from the previous case: they prefer the three directions parallel to the bonds.

Figures 3(c) and 3(d) show the bare susceptibilities χ_q^0 corresponding to the $1/4$ - and $3/4$ -filling cases, respectively. We take $\mu = -2$ and $T = 0.05$ in Fig. 3(c), and $\mu = 2$ and $T = 0.01$ in Fig. 3(d); $N = 600^2$ in both cases. For both fillings, χ_q^0 exhibits distinct peaks at the M points in the 1st BZ, consistent with the emergence of the triple-Q order. However, the wave number dependences around the peaks are totally different from each other. In the case of $1/4$ filling, the peak of χ_q^0 is broader along the direction A compared to the perpendicular direction B, as shown in Fig. 3(c). In contrast, in the case

of 3/4 filling, the peak of $\chi_{\mathbf{q}}^0$ is much sharper along the direction A than B, as shown in Fig. 3(d). To show the anisotropic structures of $\chi_{\mathbf{q}}^0$ near the peaks more clearly, we present the enlarged figures in the three-dimensional style in Figs. 3(e) and 3(f), corresponding to the white dashed areas in Figs. 3(c) and 3(d), respectively. We will discuss the relation between the wave number dependences of $\chi_{\mathbf{q}}^0$ and the distinct preferences in the direction of DWs in Sec. IV.

Besides the direction of the DWs, we note that the width of DWs is different between the two cases [see also Figs. 4(d) and 4(f)]. The difference presumably stems from the different electronic structures. The triple- Q state is metallic for the parameters used in Fig. 3(a), whereas it is insulating for Fig. 3(b). DWs might be thicker in the metallic system than the insulating one, reflecting the difference of the correlation length of electrons through the spin-charge coupling.

The difference is more directly observed in the electronic properties. As the triple- Q AFM states are ferroic ordered states of the spin scalar chirality, they exhibit spontaneous electric currents at the edges of the system due to the spin Berry phase mechanism⁴⁷. Such edge currents also appear at the DWs. Figures 4(a) and 4(b) show the real-space distributions of the local current density corresponding to the spin states in Figs. 3(a) and 3(b), respectively, obtained by the method in Sec. II D. Here, the local current density is defined as

$$j_k^\nu = \frac{1}{2i} \langle \hat{c}_k^\dagger \hat{c}_l - \hat{c}_l^\dagger \hat{c}_k \rangle, \quad (23)$$

where k and l are the nearest-neighbor sites along the ν direction ($\nu = 1, 2, 3$), as shown in the inset of Fig. 4(a). The color of each bond represents j_i^ν defined on the bond. As shown in Fig. 4(a) for the case of 1/4 filling, the electric current flows in a (counter)clockwise direction in the domains with positive (negative) χ_p^{sc} . On the other hand, as shown in Fig. 4(b), the current flows in an opposite direction in the case of 3/4 filling. The directional difference is explained by the Berry curvature of the occupied bands at each filling^{28,29}. More interestingly, the two cases show a large difference in the spatial distribution of the current density. In the case of 1/4 filling, the current density is distributed in a wide region in each domain, but in the case of 3/4 filling, it is spatially limited to the vicinity of the DWs. This is presumably because the influence of DWs spreads over a wider range in the 1/4-filling metallic state than the 3/4-filling insulating one as the electron correlation length is longer in the former metallic case than the latter insulating case, as mentioned above for the thickness of the DWs.

Let us look closer how the current density and spin scalar chirality change near DWs. Figure 4(c) shows the enlarged figure of Fig. 4(a) in the square region, where a vertical DW runs in the vertical direction in the center of the square [see Fig. 3(a)]. We plot the projected current density and spin scalar chirality along the arrow A in Fig. 4(c). Here, we define the projected current density

at site i , j_i , by the sum of j_k^ν projected onto the upward direction along the DW [perpendicular to A in Fig. 4(c)]; we take the sum of the projected j_k^ν over six bonds connected to the site i . We also define the averaged scalar chirality at site i , χ_i^{sc} , as the average of the spin scalar chirality on the six plaquettes including the site i . Figure 4(d) shows the profiles of j_i and χ_i^{sc} along the cut A in Fig. 4(c). The result indicates that χ_i^{sc} changes smoothly from positive to negative across the DW, and j_i exhibits a broad negative peak where χ_i^{sc} is suppressed. j_i has a nonzero value over about ten sites around the DW, while it shows bumpy behavior presumably due to statistical fluctuations of the small quantity. The corresponding plots for the 3/4-filling case are shown in Figs. 4(e) and 4(f). In this case, χ_i^{sc} changes rather sharply near the DW, and correspondingly, the negative peak of j_i is much sharper than that in the 1/4-filling case; j_i decays to zero much quicker than that in Fig. 4(c). We also note that the absolute value of j_i at the DW is two orders of magnitude larger than that in Fig. 4(d).

In the case of the triple- Q state at 3/4 filling, we note that the current near the DWs flows in the zigzag way, as shown in the enlarged figure in Fig. 4(e); the local currents are relatively small on the bonds along the DW direction, while they have substantial values along the other two directions near the DWs. This is because the localized spins are almost antiparallel on the bonds along the DWs, which suppresses the kinetic motion of mobile charges along this direction.

IV. DIRECTIONAL PREFERENCE OF DOMAIN WALLS

In the previous section, we found that the magnetic DWs may show directional preferences in some cases. In this section, we discuss the relationship between the structure of the bare susceptibility $\chi_{\mathbf{q}}^0$ and the directional preference of DWs.

Suppose the system shows a peak in $\chi_{\mathbf{q}}^0$ at $\mathbf{q} = \mathbf{q}^*$ and a helical ordered state with the ordering wave vector \mathbf{q}^* is realized in the ground state. The following argument is straightforwardly generalized to the cases with multiple wave vectors, e.g., the triple- Q states. In the helical ordered state, a typical spin pattern with a single DW can be described by a superposition of two helices, $\mathbf{q}^* + d\mathbf{q}$ and $\mathbf{q}^* - d\mathbf{q}$, with equal weights, where $d\mathbf{q}$ described a small deviation from \mathbf{q}^* . This DW state exhibits two pairs of Bragg peaks in the spin structure factor as

$$|\mathbf{S}_{\mathbf{q}}| = \begin{cases} \sqrt{N}/2 & (\mathbf{q} = \pm \mathbf{q}^* \pm d\mathbf{q}) \\ 0 & (\text{otherwise}). \end{cases} \quad (24)$$

Note that $\mathbf{S}_{\mathbf{q}}$ satisfies the sum rule $\sum_{\mathbf{q}} |\mathbf{S}_{\mathbf{q}}|^2 = N$. The free energy of the RKKY interaction for the DW state is

evaluated as

$$\begin{aligned}\mathcal{F}_{\text{DW}} &= -\frac{J^2}{2} (\chi_{\mathbf{q}^*+\mathbf{d}\mathbf{q}}^0 \mathbf{S}_{\mathbf{q}^*+\mathbf{d}\mathbf{q}} \cdot \mathbf{S}_{-\mathbf{q}^*-\mathbf{d}\mathbf{q}} \\ &\quad + \chi_{\mathbf{q}^*-\mathbf{d}\mathbf{q}}^0 \mathbf{S}_{\mathbf{q}^*-\mathbf{d}\mathbf{q}} \cdot \mathbf{S}_{-\mathbf{q}^*+\mathbf{d}\mathbf{q}}) \\ &= -\frac{J^2 N}{8} (\chi_{\mathbf{q}^*+\mathbf{d}\mathbf{q}}^0 + \chi_{\mathbf{q}^*-\mathbf{d}\mathbf{q}}^0). \quad (25)\end{aligned}$$

Suppose this can be expanded by the small $\mathbf{d}\mathbf{q}$, we obtain

$$\mathcal{F}_{\text{DW}} = -\frac{J^2 N}{4} \left(\chi_{\mathbf{q}^*}^0 + \frac{1}{2} \frac{d^2 \chi_{\mathbf{q}}^0}{d\mathbf{q}^2} \bigg|_{\mathbf{q}=\mathbf{q}^*} d\mathbf{q}^2 + \mathcal{O}(d\mathbf{q}^3) \right). \quad (26)$$

Note that the contribution linear to $d\mathbf{q}$ vanishes because $d\chi_{\mathbf{q}}^0/d\mathbf{q} = 0$ at $\mathbf{q} = \mathbf{q}^*$. The first term in Eq. (26) corresponds to the RKKY energy of the helical ordered state without the DW. Hence, the second term in Eq. (26) describes the leading contribution from the DW. Equation (26) indicates that the creation of the DW always requires an energy cost as the second derivative of $\chi_{\mathbf{q}}^0$ with respect to \mathbf{q} is always negative at $\mathbf{q} = \mathbf{q}^*$ by definition as long as $\chi_{\mathbf{q}}^0$ is differentiable with respect to \mathbf{q} . The energy cost is minimized when we choose $d\mathbf{q}$ along the direction where $|d^2 \chi_{\mathbf{q}}^0/d\mathbf{q}^2|$ at $\mathbf{q} = \mathbf{q}^*$ becomes smallest. This suggests that the DW has a preference in the direction along which the peak of $\chi_{\mathbf{q}}^0$ decays most slowly.

The simple analysis well explains the numerical results obtained in Sec. III. For Néel and 120° states in Secs. III A and III B, $\chi_{\mathbf{q}}^0$ is rather isotropic in the momentum space, as shown in Figs. 1(b) and 2(b). Indeed, the values of $d^2 \chi_{\mathbf{q}}^0/d\mathbf{q}^2$ in the directions A and B are in the same order. This explains the fact that the DWs in these two states do not show a strong preference in their directions. As mentioned in Sec. III A, we noted that in the Néel case there is a small preference along the diagonal directions. This is also consistent with the fact that $d^2 \chi_{\mathbf{q}}^0/d\mathbf{q}^2$ in the B direction is smaller than that in the A direction, as shown in Fig. 1(b). On the other hand, for the triple- Q states discussed in Sec. III C, $\chi_{\mathbf{q}}^0$ has strongly anisotropic structure, as shown in Figs. 3(c)-3(f). The anisotropy depends on the electron filling, which well explains the distinct preference of the DW directions found in the numerical simulations. In the 1/4-filling case, $|d^2 \chi_{\mathbf{q}}^0/d\mathbf{q}^2|$ along the direction A is about ten times smaller than B. This explains the reason why the DWs prefer the perpendicular directions to the nearest-neighbor bonds of the triangular lattice. Meanwhile, in the 3/4-filling case, $|d^2 \chi_{\mathbf{q}}^0/d\mathbf{q}^2|$ along A is more than 100 times larger than B, which is consistent with the formation of DWs along the bonds.

Let us make two remarks on the simple analysis in Eq. (26). The first one is on the expansion of $\chi_{\mathbf{q}}^0$ with respect to $d\mathbf{q}$. In some cases, $\chi_{\mathbf{q}}^0$ has a singular form with the δ functional peak at $\mathbf{q} = \mathbf{q}^*$ in the zero-temperature limit. This occurs when the system is at the van Hove singularity with $\mathbf{q} = \mathbf{q}^*$. In fact, this is the case for the Néel state and the 3/4-filling triple- Q state. Even in

these cases, the simple analysis above may be applicable, as the singularity is smeared out at finite temperatures and the DWs obey the energetics in Eq. (26) through the development of $\chi_{\mathbf{q}}^0$ while the annealing procedure.

The second point is on the higher-order contributions beyond RKKY. In the case of the triple- Q states discussed in Sec. III C, we note that the contributions beyond the RKKY interaction plays an essential role in their stabilization mechanism⁴⁵. Such beyond-RKKY contributions, however, are irrelevant in the directional preference of DWs, as the DW states with multiple- Q ordering are also described by a superposition of the multiple- Q states and the similar argument to the single- Q helical state will apply to the states. On the other hand, the higher-order contributions will play a role in the spatial patterns of the spin texture near DWs. This needs more careful analysis, which is out of scope of the present study.

V. SUMMARY

To summarize, we have investigated the formation of magnetic DWs through the spin-charge coupling by large-scale numerical simulation. We have studied the collinear Néel, coplanar 120° , and noncoplanar triple- Q states in the Kondo lattice model with classical magnetic moments by the modified KPM-LD simulation at zero temperature starting from a random spin configuration, corresponding to the sudden quench. Although neither the Néel nor 120° state shows a strong preference in the direction of DWs, the triple- Q states near 1/4 and 3/4 fillings exhibit distinct directional preferences depending on the filling. In the 1/4-filling case, DWs run dominantly along the directions perpendicular to the nearest-neighbor bonds of the triangular lattice, while in the 3/4-filling case, they strongly favor the directions parallel to the bonds, as observed in the previous study²⁷. We clarified that the directional preference of magnetic DWs in the weak-coupling region is predominantly determined by the electronic structure of mobile charges. This is rationalized by the fact that, in the weak-coupling region, the effective magnetic interaction, the so-called RKKY interaction, is given by the bare susceptibility $\chi_{\mathbf{q}}^0$, which is determined by the electronic band structure and the electron filling. While the ordering wave vector is determined by the peak of $\chi_{\mathbf{q}}^0$, we found that the directional preference of DWs is related with the wave-number dependence around the peak. When $\chi_{\mathbf{q}}^0$ is nearly isotropic around the peak, DWs have overall round shapes. On the other hand, if $\chi_{\mathbf{q}}^0$ has distinct anisotropy, the directions along which the peak of $\chi_{\mathbf{q}}^0$ decays most slowly correspond to the directions strongly preferred by DWs. The former occurs in the collinear Néel and coplanar 120° states, and the latter in the two noncoplanar triple- Q states. In particular, in the triple- Q states, $\chi_{\mathbf{q}}^0$ shows the anisotropy in a different manner between the 1/4- and 3/4-filling states, which is reflected in the different preference of the DW directions.

In the noncoplanar triple- Q states near $1/4$ and $3/4$ fillings, we have calculated the spontaneous currents induced along the DWs through the spin Berry phase mechanism. We confirmed that, reflecting the opposite sign of the Chern numbers, the current flows in the opposite directions at $1/4$ and $3/4$ fillings, as predicted in the previous studies^{28,29}. In addition, we found that the current density is spatially distributed in a wide region in the $1/4$ -filling case, while it is rather confined in the vicinity of DWs in the $3/4$ -filling case. We observed the similar tendency in the width of the magnetic DWs (the region in which the triple- Q order is disturbed); the width of DWs is thicker in the $1/4$ -filling case than the $3/4$ -filling case. The distinct behavior is presumably explained by the difference in the electronic states. The former is metallic, while the latter is insulating; the electron correlation length is longer in the former, which affects the electronic and magnetic properties in a wider region around the DWs.

Our analysis provides a simple mechanism of the directional preference of magnetic DWs in itinerant magnets. In this mechanism, the shapes of magnetic DWs are largely affected by the electronic band structure of mobile charges. In other words, our mechanism is based on the momentum-space (itinerant) picture, which is different from that by the conventional real-space (localized)

picture originating from the crystalline shape, magnetic anisotropy, and so on. As mentioned in Sec. I, recently, the interesting magnetic DWs were observed in several itinerant magnets showing metal-insulator transitions with peculiar magnetic ordering, such as $\text{Cd}_2\text{Os}_2\text{O}_7$ ¹⁹ and $\text{Nd}_2\text{Ir}_2\text{O}_7$ ²⁶. The present mechanism, which takes the effect of mobile charges into account, might offer an insight into the DW formation in such systems.

ACKNOWLEDGMENTS

The authors thank M. Udagawa for fruitful discussions in the early stage of the present study. The modified KPM-LD simulations were carried out at the Supercomputer Center, Institute for Solid State Physics, University of Tokyo. R.O. is supported by the Japan Society for the Promotion of Science through a research fellowship for young scientists and the Program for Leading Graduate Schools (ALPS). K.B. acknowledges support from the LANL Laboratory Directed Research and Development program, project #20140458ER. This research was supported by KAKENHI (No. 24340076), the Strategic Programs for Innovative Research (SPIRE), MEXT, and the Computational Materials Science Initiative (CMSI), Japan.

-
- ¹ C. Kittel, *Rev. Mod. Phys.* **21**, 541 (1949).
 - ² S. Chikazumi and C. D. Graham, 94 (Oxford University Press on Demand, 2009).
 - ³ R. Bozorth, *Journal of Applied Physics* **8**, 575 (1937).
 - ⁴ K. Hong and N. Giordano, *Phys. Rev. B* **51**, 9855 (1995).
 - ⁵ J. F. Gregg, W. Allen, K. Ounadjela, M. Viret, M. Hehn, S. M. Thompson, and J. M. D. Coey, *Phys. Rev. Lett.* **77**, 1580 (1996).
 - ⁶ G. Tatara and H. Fukuyama, *Phys. Rev. Lett.* **78**, 3773 (1997).
 - ⁷ P. M. Levy and S. Zhang, *Phys. Rev. Lett.* **79**, 5110 (1997).
 - ⁸ G. Tatara, H. Kohno, and J. Shibata, *Physics Reports* **468**, 213 (2008), ISSN 0370-1573.
 - ⁹ J. Přívratská, B. Shaparenko, V. Janovec, and D. Litvin, *Ferroelectrics* **269**, 39 (2002).
 - ¹⁰ J. Seidel, L. W. Martin, Q. He, Q. Zhan, Y.-H. Chu, A. Rother, M. Hawkrige, P. Maksymovych, P. Yu, M. Gajek, et al., *Nature materials* **8**, 229 (2009).
 - ¹¹ A. Yamaguchi, T. Ono, S. Nasu, K. Miyake, K. Mibu, and T. Shinjo, *Phys. Rev. Lett.* **92**, 077205 (2004).
 - ¹² M. Yamanouchi, D. Chiba, F. Matsukura, and H. Ohno, *Nature* **428**, 539 (2004).
 - ¹³ J. Slonczewski, *J. Magn. Magn. Mater.* **159**, L1 (1996), ISSN 0304-8853.
 - ¹⁴ N. Sedlmayr, V. K. Dugaev, and J. Berakdar, *Phys. Rev. B* **83**, 174447 (2011).
 - ¹⁵ J. Zang, M. Mostovoy, J. H. Han, and N. Nagaosa, *Phys. Rev. Lett.* **107**, 136804 (2011).
 - ¹⁶ L. Berger, *Phys. Rev. B* **54**, 9353 (1996).
 - ¹⁷ M. Kläui, P.-O. Jubert, R. Allenspach, A. Bischof, J. A. C. Bland, G. Faini, U. Rüdiger, C. A. F. Vaz, L. Vila, and C. Vouille, *Phys. Rev. Lett.* **95**, 026601 (2005).
 - ¹⁸ J. Iwasaki and N. Nagaosa, *J. Phys. Soc. Jpn.* **84**, 083701 (2015).
 - ¹⁹ S. Tardif, S. Takeshita, H. Ohsumi, J.-i. Yamaura, D. Okuyama, Z. Hiroi, M. Takata, and T.-h. Arima, *Phys. Rev. Lett.* **114**, 147205 (2015).
 - ²⁰ X. Wan, A. M. Turner, A. Vishwanath, and S. Y. Savrasov, *Phys. Rev. B* **83**, 205101 (2011).
 - ²¹ Y. Yamaji and M. Imada, *Phys. Rev. X* **4**, 021035 (2014).
 - ²² Y. Yamaji and M. Imada, *Phys. Rev. B* **93**, 195146 (2016).
 - ²³ K. Matsuhira, M. Tokunaga, M. Wakeshima, Y. Hinatsu, and S. Takagi, *J. Phys. Soc. Jpn.* **82**, 023706 (2013).
 - ²⁴ K. Ueda, J. Fujioka, Y. Takahashi, T. Suzuki, S. Ishiwata, Y. Taguchi, M. Kawasaki, and Y. Tokura, *Phys. Rev. B* **89**, 075127 (2014).
 - ²⁵ K. Ueda, J. Fujioka, C. Terakura, and Y. Tokura, *Phys. Rev. B* **92**, 121110 (2015).
 - ²⁶ E. Y. Ma, Y.-T. Cui, K. Ueda, S. Tang, K. Chen, N. Tamura, P. M. Wu, J. Fujioka, Y. Tokura, and Z.-X. Shen, *Science* **350**, 538 (2015), ISSN 0036-8075.
 - ²⁷ K. Barros and Y. Kato, *Phys. Rev. B* **88**, 235101 (2013).
 - ²⁸ I. Martin and C. D. Batista, *Phys. Rev. Lett.* **101**, 156402 (2008).
 - ²⁹ Y. Akagi and Y. Motome, *J. Phys. Soc. Jpn.* **79**, 083711 (2010).
 - ³⁰ D. Loss, D. P. DiVincenzo, and G. Grinstein, *Phys. Rev. Lett.* **69**, 3232 (1992).
 - ³¹ J. Ye, Y. B. Kim, A. J. Millis, B. I. Shraiman, P. Majumdar, and Z. Tešanović, *Phys. Rev. Lett.* **83**, 3737 (1999).
 - ³² C. Zener, *Phys. Rev.* **82**, 403 (1951).
 - ³³ P. W. Anderson and H. Hasegawa, *Phys. Rev.* **100**, 675

- (1955).
- ³⁴ M. A. Ruderman and C. Kittel, Phys. Rev. **96**, 99 (1954).
- ³⁵ T. Kasuya, Prog. Theor. Phys. **16**, 45 (1956).
- ³⁶ K. Yosida, Phys. Rev. **106**, 893 (1957).
- ³⁷ A. Weiße, G. Wellein, A. Alvermann, and H. Fehske, Rev. Mod. Phys. **78**, 275 (2006).
- ³⁸ Z. Wang, C. D. Batista, and K. Barros, in preparation.
- ³⁹ J. M. Tang and Y. Saad, Numer. Linear Algebra Appl. **19**, 485 (2012).
- ⁴⁰ B. Skubic, J. Hellsvik, L. Nordstrom, and O. Eriksson, Journal of Physics: Condensed Matter **20**, 315203 (2008).
- ⁴¹ J. H. Mentink, M. V. Tretyakov, A. Fasolino, M. I. Katsnelson, and T. Rasing, J. Phys.: Condens. Matter **22**, 176001 (2010).
- ⁴² S. Yunoki, J. Hu, A. L. Malvezzi, A. Moreo, N. Furukawa, and E. Dagotto, Phys. Rev. Lett. **80**, 845 (1998).
- ⁴³ The value of $\Delta\tau$ is chosen to ensure the convergence by satisfying $1/\Delta\tau > |\mathbf{H}_i| \sim \mathcal{O}(J^2)$.
- ⁴⁴ L.-W. Wang and A. Zunger, Phys. Rev. Lett. **73**, 1039 (1994).
- ⁴⁵ Y. Akagi, M. Udagawa, and Y. Motome, Phys. Rev. Lett. **108**, 096401 (2012).
- ⁴⁶ S. Hayami and Y. Motome, Phys. Rev. B **90**, 060402 (2014).
- ⁴⁷ R. Ozawa, M. Udagawa, Y. Akagi, and Y. Motome, J. Phys. Soc. Jpn. **83**, 073706 (2014).

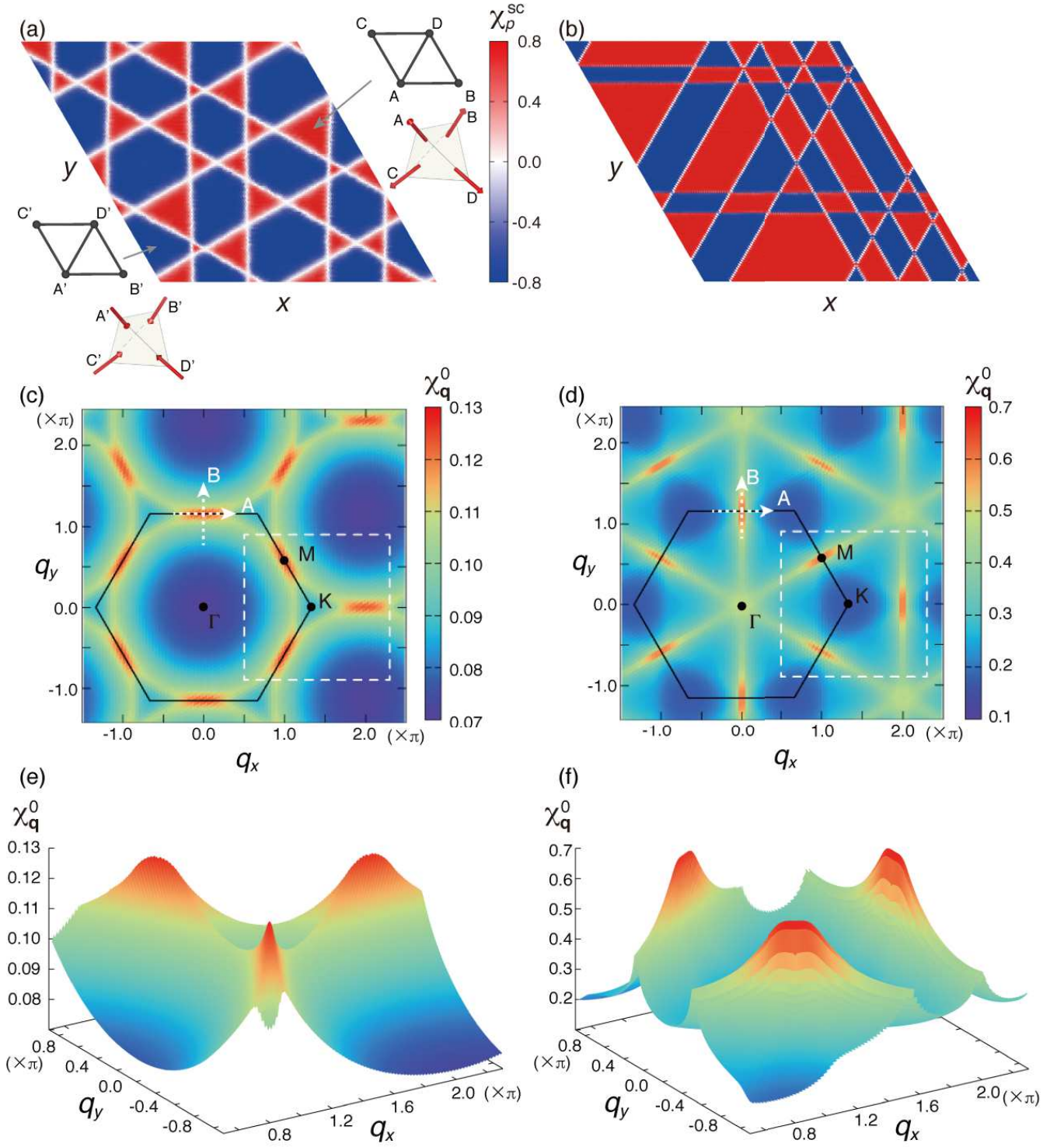


FIG. 3. (Color online) Real-space distributions of spin scalar chirality χ_p^{sc} obtained by the modified KPM-LD simulation on the triangular lattice for $J = 0.2$, $D = 0$, $N = 120^2$, and (a) $\mu = -2$ ($n \sim 0.22$) and (b) $\mu = 2$ ($n \sim 0.75$). The inset in (a) shows the schematic pictures of spin patterns in the noncoplanar triple- Q states, corresponding to the positive and negative χ_p^{sc} domains. The arrows at the corners of the tetrahedra represent the spin directions at the corresponding sites. Bare susceptibilities χ_q^0 for (c) $\mu = -2$ and (d) $\mu = 2$. The black hexagon represents the 1st BZ in each figure. The arrows A and B show the cuts along which we evaluate the second derivative of χ_q^0 ; see Sec. IV for details. (e), (f) Three-dimensional plots of χ_q^0 in the dashed squares in (c) and (d), respectively.

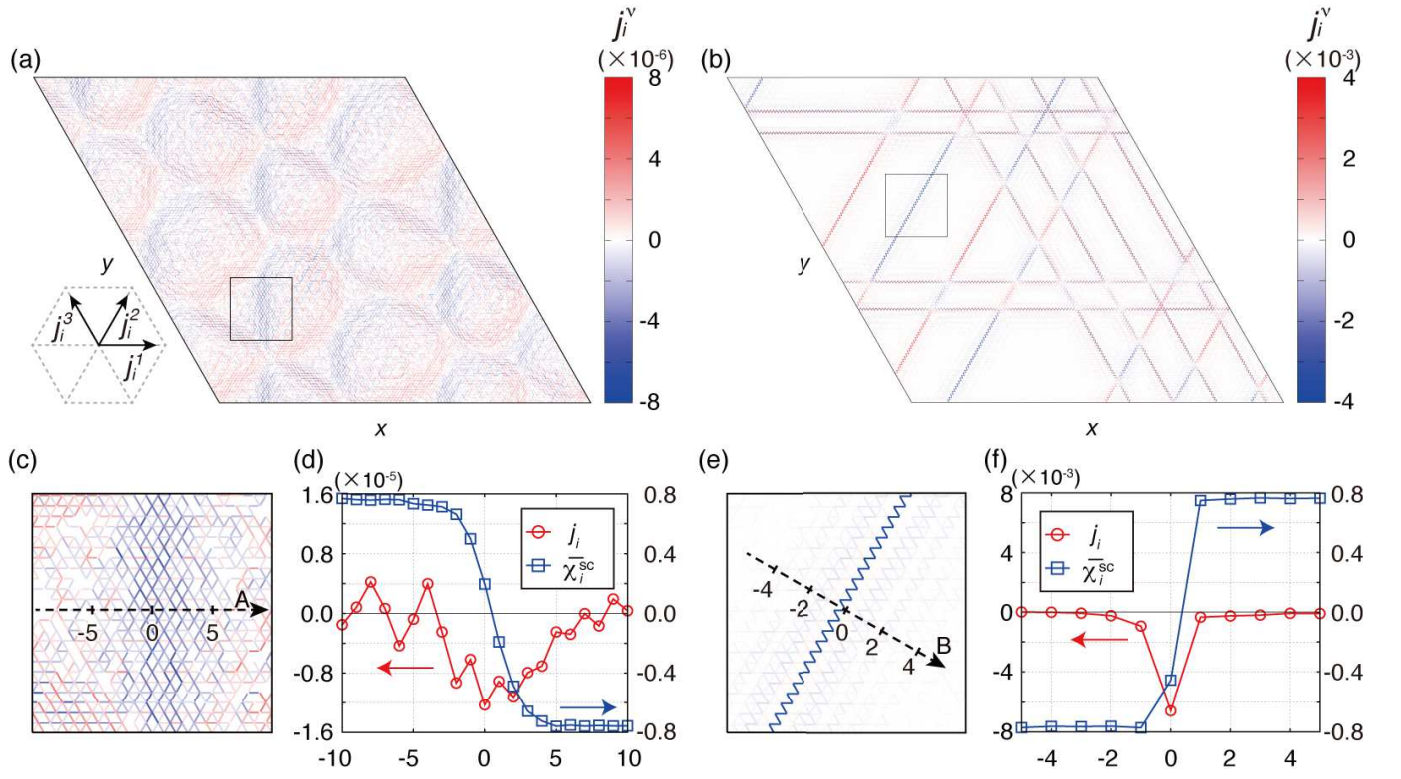


FIG. 4. (Color online) (a), (b) Real-space distributions of the local current density j_i^ν on each bond for the spin configurations in Figs. 3(a) and 3(b), respectively. (c), (e) Enlarged pictures of the square areas in (a) and (b), respectively. (d), (f) Current density j_i and spin scalar chirality χ_i^{sc} plotted along the arrows A and B in (c) and (e), respectively; see the text for details.